A model for multi-view ultrasonic array inspection of small two-dimensional defects

Nicolas Budyn, Rhodri L. T. Bevan, Jie Zhang, Anthony J. Croxford, Paul D. Wilcox

***Abstract*—The multi-view total focusing method (TFM) is an imaging algorithm for ultrasonic full matrix array data that exploits internal reflections and mode conversions in the inspected object to create multiple images, the views. Modelling the defect response in multi-view TFM is an essential first step in developing new detection and characterisation methods which exploit the information present in these views. This paper describes a ray-based forward model for small two-dimensional defects and compares its results against finite-element simulations and experimental data for the inspection of a side-drilled hole, a notch and a crack. A simpler version of this model, based on a single-frequency approximation, is derived and compared. A good agreement with the multi-frequency model and a speed-up of several orders of magnitude are achieved.**

***Index Terms*—Array signal processing, acoustic propagation, modelling, phased arrays, ultrasonic imaging, ultrasonic transducer arrays.**

I. Introduction

Ultrasonic arrays are commonly used in industrial non-destructive evaluation (NDE) for a wide range of applications [1]. Post-processing the Full Matrix Capture (FMC) data (also referred to as multistatic response matrix [2] or full array response matrix [3]), which contains the time traces corresponding to each pair of transmitter and receiver, is an active area of research. A common approach, the Total Focusing Method (TFM) synthetically focuses the wave front at every point of a grid to form an image [4]. The multi-view Total Focusing Method, also known as multi-modal TFM[1], is an extension that exploits internal reflections and mode conversions to create multiple image views from the same FMC dataset [5]. Various investigations have demonstrated the suitability and the overall good performance of multi-view TFM for the inspection of notches, cracks, side-drilled holes and welds [5]–[12]. Using an amplitude drop measurement technique in multi-view TFM images, accurate and reliable sizing of notches larger than 2 wavelengths was obtained [9], [10]. Other algorithms such as MUSIC [13] and plane wave imaging [14], plane wave with phase coherence imaging [15] have also been successfully adapted to multi-view imaging.

The authors are interested in data fusion across multiple TFM views to improve the detectability and characterisation of defects. For the detection problem, the location of the defect is *a priori* unknown (if there is one), so any position in any view is considered as a potential defect. The response of a defect greatly varies with factors that include (i) the type and size of defect, (ii) the view, (iii) the position of the defect within the view, (iv) the exact setup (e.g. probe position relative to the specimen, specimen geometry, specimen and couplant ultrasonic velocities, specimen thickness). Consequently, the response of a defect may be strong in a view but weak in another, so it is needed to determine which positions in which views are likely to contain useful information and which are not. The authors therefore desire a fast way of estimating the defect response at all positions in all views for a given setup.

This paper focuses on modelling the ultrasonic response of a small two-dimensional scatterer and in particular its maximum TFM intensities across different views. Various modelling techniques are suitable, including finite element method (FEM) and analytical models such as the commercial software CIVA UT [16]. The aim of the current work is to calculate the TFM intensities of a defect with an even higher computational efficiency for small defects, as it is an essential first step to develop new defect detection and characterisation techniques. This is done by deriving an estimator of the TFM intensities from an analytical model. First, this paper describes a frequency-domain ray-based linear time-invariant (LTI) two-dimensional forward model for efficiently predicting the intensity of multi-view TFM

This work was supported by the UK Engineering and Physical Sciences Research Council (EPSRC) [grant number EP/N015924/1]; the UK Research Centre in NDE (RCNDE); BAE Systems; EDF Energy; Hitachi; and Wood Group (formerly, Amec Foster Wheeler UK).

The authors are with the Department of Mechanical Engineering, University of Bristol, Bristol, BS8 1TR, UK (e-mail: n.budyn@.bristol.ac.uk).

[1]The authors prefer the term *multi-view* over *multi-mode* because the latter also refers to nondestructive inspections with different techniques (ultrasonic, eddy current, radiography testing, etc.).

images with arbitrarily-shaped defects at any location. Then, the model is validated against experimental and finite-element data for a side-drilled hole, a crack and a notch. Finally, a simpler and significantly faster single-frequency version is derived for even higher computational efficiency and is compared.

A. Inspection configuration

The inspection configuration shown in 1a approximates a common NDE scenario where the fusion of multi-view TFM could lead to significant improvements in automated defect detection and characterisation: the inspection of the fusion face of a weld. The ultrasonic array is held at a distance from and inclined relative to the top surface of the specimen to ensure good generation of longitudinal and transverse waves. The region of interest, where defects may occur, is not directly below the array. Both the inspected object and the array are immersed in water. The specimen is a homogeneous isotropic metal block. The top and bottom surfaces (front and back walls) are planar.

B. Multi-view imaging

Multi-view imaging considers various ray paths between the ultrasonic array and a grid of points to form multiple images of the same physical region of interest in the examination object. Figure 1 shows the 6 paths considered in this paper, with zero or one internal reflection against the back wall and with longitudinal (L) and transverse (T) waves: L, T, LL, LT, TL, TT. For conciseness, the L mode in water is not included in the description of the path as this is the only mode supported in a fluid. In the transmission nomenclature (transmitter–image point), the modes are read from the probe to the image point. In the reception nomenclature (image point–receiver), the modes are read from the image point to the probe. The full ray paths, transmitter–image point–receiver, are obtained by the combination of a transmit path and a receive path from these six. For example, the full path L–TL corresponds to the L path in transmission and TL path in reception (scattered T wave and mode conversion T to L against the back wall).

In multi-view imaging, each full path is used to create a view. Because the FMC matrix is symmetrical due to the reciprocity of linear elastodynamics, algorithms based only on the times of flight, such as TFM, produce redundant views [17]. From these 6 paths, 21 views are unique out of a total of 36.

II. Model description

A. Overview

The model predicts the scatterer response for every transmitter and receiver pair during the immersion inspection of a homogeneous isotropic object. This is an adaptation of the linear time-invariant (LTI) model developed by Thompson and Gray [18] and Schmerr [19] to the multi-view immersion inspection. The contribution of the scatterer to the time trace is calculated in three main steps: (1) the calculation of the incident wave amplitudes on the scatterer (transmit path), (2) the calculation of the scattering and (3) the calculation of the wave amplitudes propagated back from the scatterer to the probe (receive path). The response of a scatterer located in the solid at point $\boldsymbol{y}$ (boldface is used to indicate vector quantities), insonified by the i-th probe element and received by the j-th element is modelled:

$$G_{ij}(\omega, \boldsymbol{y}) \coloneqq P_{ij}(\omega, \boldsymbol{y}) e^{\iota\omega \mathcal{T}_{ij}(\boldsymbol{y})} U(\omega) \tag{1}$$

with

$$P_{ij}(\omega, \boldsymbol{y}) \coloneqq T_i(\boldsymbol{y}) T'_j(\boldsymbol{y}) B_i(\boldsymbol{y}) B'_j(\boldsymbol{y}) \\ D_i(\omega, \boldsymbol{y}) D'_j(\omega, \boldsymbol{y}) S_{ij}(\omega, \boldsymbol{y})$$

where:

- $T_i(\boldsymbol{y})$ and $T'_j(\boldsymbol{y})$ encapsulate the real or complex plane wave transmission and reflection coefficients at the relevant fluid-solid interfaces encountered on respectively the transmit and receive paths [19];
- $B_i(\boldsymbol{y})$ and $B'_j(\boldsymbol{y})$ describe the geometrical attenuation (beam-spread) for respectively the transmit and receive paths;
- $D_i(\omega, \boldsymbol{y})$ and $D'_j(\omega, \boldsymbol{y})$ are the directivity of the probe elements associated with the transmit and receive path directions in the couplant relative to the probe;
- $S_{ij}(\omega, \boldsymbol{y})$ is the scattering amplitude;
- $\mathcal{T}_{ij}(\boldsymbol{y})$ is the time of flight of the total ray path;
- $U(\omega)$ is the ultrasonic toneburst.

Details about these terms are given below. Except $U(\omega)$, all these quantities are view-dependent. All elements are assumed to emit the same signal $U(\omega)$. The wave amplitudes are described by pressure in the fluid and displacement in the solid. The material attenuation in the samples considered in this paper is too low to give any significant difference, so it is ignored; it could however be accounted for if need be.

a) Scattering: Under the assumption that the incident wavefront is planar and of constant amplitude over the extent of the defect (i.e. quasi-plane wave insonification), the defect response can be approximated

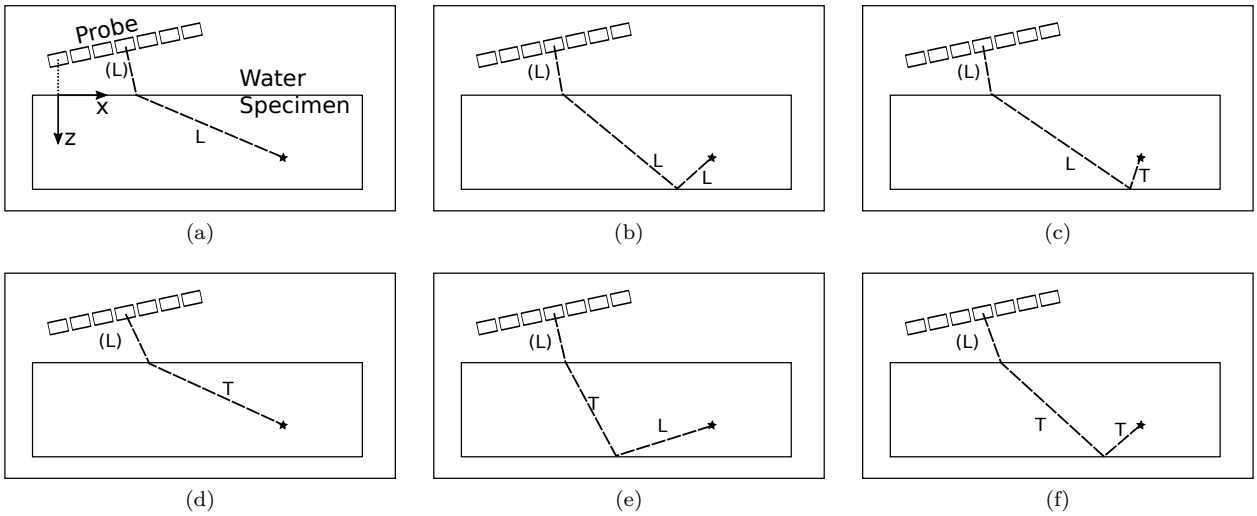

Figure 1. The ray paths considered between the an array element and an image point described using transmission nomenclature: (a) L, (b) LL, (c) LT, (d) T, (e) TL, (f) TT. In reception nomenclature, the modes are read from the image point instead of from the array. In both cases, the L mode in water is omitted from the path nomenclature for brevity.

by the infinite medium scattering amplitudes [18] [19, §10.1.1]. In other words, the inspection-specific calculation of the flaw response comes down to its calculation in the canonical case of a scatterer in an unbounded medium with an incident plane wave of unit amplitude. More specifically, the scattering amplitudes are defined as the ratio of the displacement of the scattered wave at an arbitrarily-chosen reference distance divided by the displacement of the incident plane wave in an unbounded medium. For a given defect, they are functions of the frequency, the incident and scattered angles.

This simplification has three main consequences. First, the abundant literature about flaw scattering in the unbounded case can be used. In particular in this work, the scattering functions are obtained analytically for a side-drilled hole [20] and a crack (finite length, infinitesimal width) [21] and finite-element analysis can be employed for arbitrary shapes of defects such as notches (finite length and width) [22]. Second, it is possible to precompute and cache the scattering amplitudes for computational efficiency. Third, it is sufficient to calculate the rays between the array elements and only one point of the defect, typically its centre. Practically, a defect is therefore modelled as a point-like scatterer with a specific frequency-dependent angular amplitude distribution which depends on its type and size because their far field scattering functions are the same.

b) Ray tracing: Calculating the ray paths between the array elements and the scatterer is an essential step because all terms in equation (1) except $U(\omega)$ depend on the geometry of the rays. The rays are calculated using Fermat's minimum-time principle [23, §7.1.3.1]. Because the medium is made up of homogeneous layers, and because the rays in a homogeneous medium are straight, ray tracing is done by finding the points at the intersecting surfaces which minimise the time of flight, similarly to previous work [5]. For simplicity of implementation, the minimisation is done numerically by discretising the surfaces and considering all possible paths (brute-force approach).

The output of the ray tracing step is the coordinates of the rays and their times of flight $\mathcal{T}_{ij}(\boldsymbol{y})$.

c) Directivity: Each element is modelled as a line-source piston (2D equivalent of a rectangular piston), which leads to the following directivity function [1], [24]:

$$D(\omega, \boldsymbol{y}) = \operatorname{sinc} \frac{\pi a \sin\theta}{\lambda}$$

where θ is the angle between the normal of the element and the ray, a is the width of the probe element and λ is the wavelength in the couplant.

d) Beam-spread: The attenuation due to the beam-spreading in an infinite medium and in two dimensions is $1/\sqrt{r}$. The beam-spread through a planar interface can be rigorously calculated using a high frequency approximation of the Rayleigh-Sommerfeld equation and the method of stationary phase [19, §8.3.1]. The ray theory method gives equivalent results [24, §2.5]. These functions are given in the appendix.

e) Ultrasonic toneburst: The ultrasonic toneburst $U(\omega)$ is the overall array response to a single reflector and encapsulates the input electrical signal and the

transmit and receive dynamics of the acquisition instrument and the probe. This term is an input of the model; an experimental measurement technique to obtain it is described in [25].

In this work, $U(\omega)$ is modelled as the Fourier transform of a Hann-windowed sine wave scaled by a single coefficient measured experimentally.

f) Single-frequency approximation: The scatterer response defined in equation (1) is rewritten to separate the frequency-independent from the frequency-dependent terms:

$$G_{ij}(\omega, \boldsymbol{y}) = P_{ij}(\omega_0, \boldsymbol{y}) Q_{ij}(\omega, \boldsymbol{y}) e^{\iota\omega\mathcal{T}_{ij}(\boldsymbol{y})} U(\omega) \tag{2}$$

with

$$Q_{ij}(\omega, \boldsymbol{y}) \coloneqq \frac{D_i(\omega, \boldsymbol{y}) D'_j(\omega, \boldsymbol{y}) S_{ij}(\omega, \boldsymbol{y})}{D_i(\omega_0, \boldsymbol{y}) D'_j(\omega_0, \boldsymbol{y}) S_{ij}(\omega_0, \boldsymbol{y})}$$

where ω_0 is the probe centre frequency. To obtain the scatterer response, the toneburst is time-shifted, then rescaled and phase-shifted by the complex coefficient $P_{ij}(\omega_0, \boldsymbol{y})$ and finally the shape and the amplitude of the toneburst are furthermore changed by the frequency-dependent coefficient $Q_{ij}(\omega, \boldsymbol{y})$. A first-order heuristic is to consider that the change of the response amplitude is mainly caused by $P_{ij}(\omega_0, \boldsymbol{y})$ whereas the frequency-dependent variation, $Q_{ij}(\omega, \boldsymbol{y})$ causes a smaller amplitude variation in comparison. Ignoring this frequency dependence leads to the single-frequency approximation:

$$G_{ij}^{\omega_0}(\omega, \boldsymbol{y}) \coloneqq P_{ij}(\omega_0, \boldsymbol{y}) e^{\iota\omega\mathcal{T}_{ij}(\boldsymbol{y})} U(\omega). \tag{3}$$

Under this approximation, the scatterer response is obtained by time-shifting and multiplying the toneburst by a single complex coefficient. The fine geometric features of the scatterer, conveyed in the frequency-dependent term, are lost. However, this single-frequency model may be useful when only a first-order amplitude estimation of the scatterer response is needed and is significantly faster to run than the multi-frequency model.

B. Sensitivity model for predicting TFM intensities

The time trace for the transmitter i and the receiver j is denoted $f_{ij}(t)$ in the time domain and $F_{ij}(\omega)$ in the frequency-domain. Similarly, the simulated response to a single scatterer at position $\boldsymbol{y}$ is denoted $g_{ij}(t, \boldsymbol{y})$ and $G_{ij}(\omega, \boldsymbol{y})$. The analytic signals obtained using the Hilbert transform are denoted with a tilde: for example, $\tilde{f}_{ij}(t)$, $\tilde{F}_{ij}(\omega)$.

For a given view, the TFM intensity at image point $\boldsymbol{r}$ is defined as

$$I_0(\boldsymbol{r}) \coloneqq \left| \sum_{i,j} a_{ij}(\boldsymbol{r}) \tilde{f}_{ij}(\mathcal{T}_{ij}(\boldsymbol{r})) \right| \tag{4}$$

where the times of flight, $\mathcal{T}_{ij}(\boldsymbol{r})$, and the arbitrary weights, $a_{ij}(\boldsymbol{r})$, are view-dependent. The weights $a_{ij}(\boldsymbol{r})$ can be used for spatial filtering [16], [26]; in the present work, uniform weighting is used ($a_{ij}(\boldsymbol{r}) = 1$).

In the vicinity of a scatterer, the TFM intensity $I_0(\boldsymbol{r})$ for a given view includes the scatterer response $g_{ij}(t, \boldsymbol{y})$ for this view (the desired signal) but may also include the scatterer response from other modes and wall echoes. These latter signals create artefacts in the images and interfere constructively or destructively with the desired scatterer response. However, because the times of arrival of the artefacts are in general different from those of the signals of interest, the artefacts are ignored here. Simulated artefact-free TFM images are obtained from the model by replacing the time trace $\tilde{f}_{ij}(t)$ by the scatterer response in the imaged view:

$$I_1(\boldsymbol{r}, \boldsymbol{y}) \coloneqq \left| \sum_{i,j} a_{ij}(\boldsymbol{r}) \tilde{g}_{ij}(\mathcal{T}_{ij}(\boldsymbol{r}), \boldsymbol{y}) \right|. \tag{5}$$

For example, the artefact-free T–T image only contains the T–T defect response. The actual T–T image contains other defect echoes such as the L–L response and wall echoes; they are absent of the artefact-free image. To reduce the computational burden, the approximation defined in equation (3) is applied to obtain the single-frequency artefact-free image for a given view:

$$I_2(\boldsymbol{r}, \boldsymbol{y}) \coloneqq \left| \sum_{i,j} a_{ij}(\boldsymbol{r}) \tilde{g}_{ij}^{\omega_0}(\mathcal{T}_{ij}(\boldsymbol{r}), \boldsymbol{y}) \right|. \tag{6}$$

Furthermore, only the intensity at a single point of the defect image, the defect centre $\boldsymbol{y}$, is considered. For $\boldsymbol{r} = \boldsymbol{y}$, the TFM intensity becomes:

$$\begin{aligned} I_2(\boldsymbol{r}, \boldsymbol{r}) &= \frac{1}{2\pi} \left| \sum_{i,j} a_{ij}(\boldsymbol{r}) \int_{-\infty}^{+\infty} \tilde{G}_{ij}^{\omega_0}(\omega, \boldsymbol{r}) e^{-\iota\omega\mathcal{T}_{ij}(\boldsymbol{r})} \, d\omega \right| \\ &= \frac{1}{\pi} \left| \sum_{i,j} a_{ij}(\boldsymbol{r}) \int_{0}^{+\infty} G_{ij}^{\omega_0}(\omega, \boldsymbol{r}) e^{-\iota\omega\mathcal{T}_{ij}(\boldsymbol{r})} \, d\omega \right| \\ &= \frac{1}{\pi} \left| \sum_{i,j} a_{ij}(\boldsymbol{r}) \int_{0}^{+\infty} P_{ij}(\omega_0, \boldsymbol{r}) U(\omega) \, d\omega \right|. \end{aligned} \tag{7}$$

Noting that $\frac{1}{\pi} \int_0^{+\infty} U(\omega) \, d\omega = \tilde{u}(0)$, the sensitivity image [17], [27] is defined as:

$$E(\boldsymbol{r}) \coloneqq I_2(\boldsymbol{r}, \boldsymbol{r}) = \left| \tilde{u}(0) \sum_{i,j} a_{ij}(\boldsymbol{r}) P_{ij}(\omega_0, \boldsymbol{r}) \right|. \tag{8}$$

For a given view, the sensitivity image, $E(\boldsymbol{r})$, represents an estimate (under the single-frequency assumption) of

the TFM intensity that would be measured if a defect of the prescribed type existed with its centre at $\boldsymbol{r}$. The quality of the estimation is discussed in a later section of this paper. This quantity requires less computation than the artefact-free TFM images $I_1(\boldsymbol{r},\boldsymbol{y})$ and $I_2(\boldsymbol{r},\boldsymbol{y})$ because (i) no frequency integration is required and (ii) the TFM algorithm is performed at a single point, the defect centre, instead of on a grid in the vicinity of the defect. One may notice that the exact form of the toneburst $U(\omega)$ is ignored in this sensitivity model because of the single-frequency assumption; only the amplitude of its envelope at $t = 0$, $|\tilde{u}(0)|$ matters and acts in practice as a scaling coefficient.

C. Time interpolation of time traces in TFM

Numerically, the TFM is usually calculated in its time-domain form (equations (4), (5) and (6)) where the time traces are linearly interpolated between time samples [4]. However, because of this linear interpolation, the intensities obtained with the time-domain forms are systematically lower than the ones obtained with the frequency-domain forms of TFM like equations (7) and (8). The magnitude of this difference depends on the sampling rate and frequency content of the signals and varies from pixel to pixel; at 25 MHz sampling rate with a nominal centre frequency of 5 MHz, it was observed to be around 2 dB. In practice, linear interpolation is generally sufficient and a heuristic correction based on the sampling rate and the ultrasonic frequency could be applied if desired; however, in order to systematically eliminate the effect of this variation from subsequent comparisons, the more accurate Lanczos interpolation [28], [29] is used in this work:

$$k(t) = \sum_{n=\lfloor t/T \rfloor - a + 1}^{\lfloor t/T \rfloor + a} k(nT) L(t/T - n) \tag{9}$$

where $1/T$ is the sampling frequency, $L(x)$ is the Lanczos kernel of order b:

$$L(x) = \begin{cases} \operatorname{sinc}(\pi x)\operatorname{sinc}(\pi x/a) & \text{if } -a < x < a, \\ 0 & \text{otherwise.} \end{cases}$$

With a kernel of order $a = 3$, the error is reduced to 0.001 dB, at the cost of a 10 times slower computation of TFM images compared to linear interpolation (CPU implementation).

III. Multi-frequency model validation

The multi-frequency model defined previously is validated in this section against experimental data and data obtained from the finite-element method (FEM) in three different cases described in Table I. The FEM data is generated using a two-dimensional hybrid model which couples (i) a similar analytical model for the wave propagation in the fluid and (ii) the Pogo solver [30] for modelling the elastic propagation and interaction inside the solid [31]. The nodes at the fluid/solid interfaces of this hybrid model act as Huygens sources for the pressure in fluid and for the vertical displacement in the solid. The material defined in the FEM simulation has the density and velocities of a copper-nickel alloy but has no material attenuation.

In the experimental datasets, each time trace is time-shifted by the instrument acquisition delay, measured by subtracting the times of arrival of two consecutive front wall echoes in normal incidence, so that the maximum amplitude of the transmitted toneburst $\tilde{u}(t)$ is obtained at $t = 0$. The probe location is calculated from the times of arrival of the front wall echo in the pulse-echo time traces. The longitudinal and transverse velocities in the sample material are obtained under the assumption that the correct values maximise the TFM intensities of the back wall echo; the block thickness being known, the longitudinal and traverse velocities are thereby obtained from the L–L and L–T views, respectively.

The time traces (experimental, FEM, simulated) are filtered with a fourth order Butterworth bandpass filter to remove potential low-frequency offsets and high-frequency noise. The filter has negligible impact on the toneburst bandwidth.

For the ray tracing, the distance between two consecutive points of the discretised interfaces is 30 µm. Compared to a twice as coarse grid, the largest observed difference of TFM defect intensities for the notch dataset was 0.02 dB, which demonstrates the interfaces are fine enough to make the error negligible.

To measure the model scaling coefficient $|\tilde{u}(0)|$, the back wall reflection for the L–L path is modelled using a ray-based approach consistent to that described above for point-like scatterers. The amplitudes of the back wall are measured by taking for each experimental/FEM time trace the maximum of the envelope of the signal near the expected time of arrival. The ratio between the modelled and the experimental back wall amplitudes is the model scaling; this ratio is assumed to be the same for all pairs of time traces. An ordinary least squares regression is performed for robustness to obtain the final model coefficient. The back wall reflected for the path L–L was chosen because it provides a strong signal, clearly visible in all time traces. In a previous work [17], the front wall reflection was used instead; however, the back wall appears to be less sensitive to small probe misalignments and

Table I
DESCRIPTION OF THE THREE VALIDATION CASES.

Dataset name	Crack	Notch	SDH
Source	FEM	Experiment	Experiment
Defect properties			
Type	crack	notch	SDH
Size	0.5 mm	3×1 mm	Ø1 mm
Orientation	110°	90° (vertical)	/
Location x (mm)	26	46	46
Location z (mm)	10	20	20
Block properties			
Material	copper nickel	aluminium	aluminium
L velocity (m/s)	5050	6384	6410
T velocity (m/s)	2534	3156	3150
L att. (Np/m)	0	0[1]	0[1]
T att. (Np/m)	0	0[1]	0[1]
Density (kg/m^3)	7800	2700[1]	2700[1]
Thickness (mm)	20	40	40
Probe properties			
Number of elements	110	64	64
Centre frequency (MHz)	5	2.5	2.5
Element pitch (mm)	0.17	0.5	0.5
Probe stand-off (mm)	17.0	29.9	29.8
Probe angle	11.0°	12.5°	12.5°
Filter passband (MHz)	2–8	1–4	1–4

[1] Not measured.

therefore provides a more robust estimation of the model scaling. A proper investigation would require a three-dimensional model to understand the effect of the out-of-plane misalignment in the front and back wall amplitudes.

A. Results

Figures 2 and 3 show the simulated and experimental/FEM defect response images in the different views on a dB scale; in each image, 0 dB corresponds to the maximum intensity in the magenta box. A good qualitative agreement is achieved: the tip diffraction and the specular reflection of the notch, and the various defect patterns are generally correctly simulated.

Figure 4 shows a quantitative absolute comparison of the maximum TFM intensities around the defect in experimental/FEM images $I_0(\boldsymbol{r})$ and simulated ones $I_1(\boldsymbol{r},\boldsymbol{y})$. The measurement area is a square of side 5 mm (magenta squares in figures 2 and 3); the pixel size is 0.25 mm. Due to computational limitations, the simulation time of the FEM data is shorter than the times of arrival of the waves in some views therefore only 12 views are available for the crack dataset. The median/standard deviation of the errors for all views are -1.7/2.4 dB (notch), 0.0/3.1 dB (SDH) and 0.1/1.5 dB (crack). For 48 views out of 54, the agreement is within ±3 dB. The defect response varies significantly between the views: a variation of 20 dB (crack), 30 dB (notch) and 36 dB (SDH) is observed between the highest and lowest TFM intensities. These large variations are correctly explained by the model.

In views where the defect response is low (approximately less than -20 dB relative to the brightest view), the defect may be hard to distinguish from the surrounding artefacts because of their similar or stronger amplitudes. In this situation, the assumption that the measured amplitude is close to the artefact-free one becomes questionable.

IV. SENSITIVITY MODEL VALIDATION

The sensitivity model defined in equation (8) provides an estimate of the TFM intensity of a defect. To assess the validity of this estimation, Figure 5 shows the absolute comparison of the sensitivity model amplitudes $E(\boldsymbol{r})$ against the maximum artefact-free multi-frequency TFM images $I_1(\boldsymbol{r},\boldsymbol{y})$ near the defect. The median/standard deviation of the errors for all views are 0.0/2.3 dB (notch), -0.1/2.3 dB (SDH) and -0.5/1.5 dB (crack). For 51 views out of 63, the agreement is within ±3 dB.

The sensitivity model assumes that the intensity at the defect centre is a good estimate of the peak intensity. This assumption falls short when the intensity at the defect centre is a trough due to a phase effect (for example in figure 2f, even though the estimate remains good in this case). The magnitude of this error between the sensitivity model and multi-frequency model depends on the view and the defect type and becomes stronger at higher frequencies. In the presented datasets, it appears particularly in the view LL-TT of the SDH. Despite this, a good agreement is achieved.

These results *a posteriori* validate the single-frequency assumption (Equation 3): the peak TFM intensities are mainly explained by a single-frequency model; the multi-frequency dependence of the model, including the scattering, has a limited effect in comparison. However, the single-frequency model is too coarse to predict features of the image such as the tip diffractions (images available in online repository): these effects can only be modelled with the finer multi-frequency model.

Figure 6 shows the predicted TFM intensities of a notch anywhere and for any view; the configuration is the same as the notch dataset described above except that 14,299 defect locations are considered. These sensitivity images exhibit large variations of intensities, both within each view and across the views. They show clearly the areas of high intensities and the blind

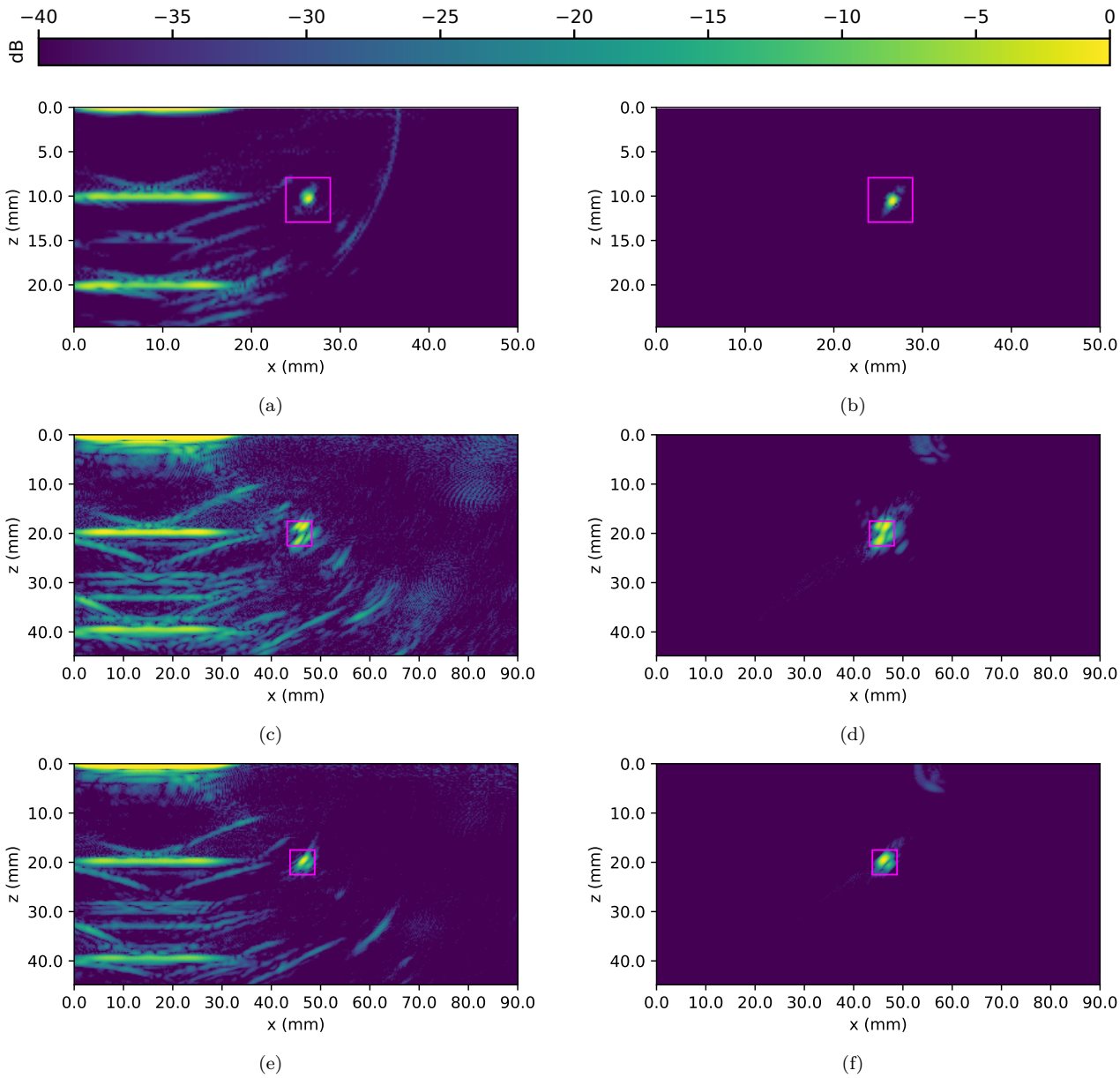

Figure 2. TFM images of view T–T. Left column: experimental images $I_0(\boldsymbol{r})$. Right column: artefact-free simulated images $I_1(\boldsymbol{r}, \boldsymbol{y})$. Top row: crack. Middle row: notch. Bottom row: SDH. In each image, 0 dB corresponds to the maximum intensity in the magenta box.

valleys, which are specific to the defect type and orientation. These images could be used to assess the suitability of an inspection configuration to detect a given defect. For example, the views L–L, LL-T and TT–T seem particularly suited to inspecting a vertical notch at $x \approx 50$mm because they provide the highest TFM intensities and because they do not exhibit strong blind spots in this area.

The advantage of the sensitivity model is its high computational efficiency. The total runtime for these 14,299 defect locations, excluding the pre-calculation of the defect scattering distributions which is performed in a first step and cached, is 75 s for 21 views on a desktop computer (Intel Core i7-4790 3.6 GHz quad-core processor; 16 GB RAM). To obtain equivalent results to the sensitivity model for 14,299 candidate defect locations, it would take 5 days using the artefact-free multi-frequency model $I_1(\boldsymbol{r}, \boldsymbol{y})$ (30 seconds per location) and 39 years with the current finite-element analysis implementation (1 day per location). The

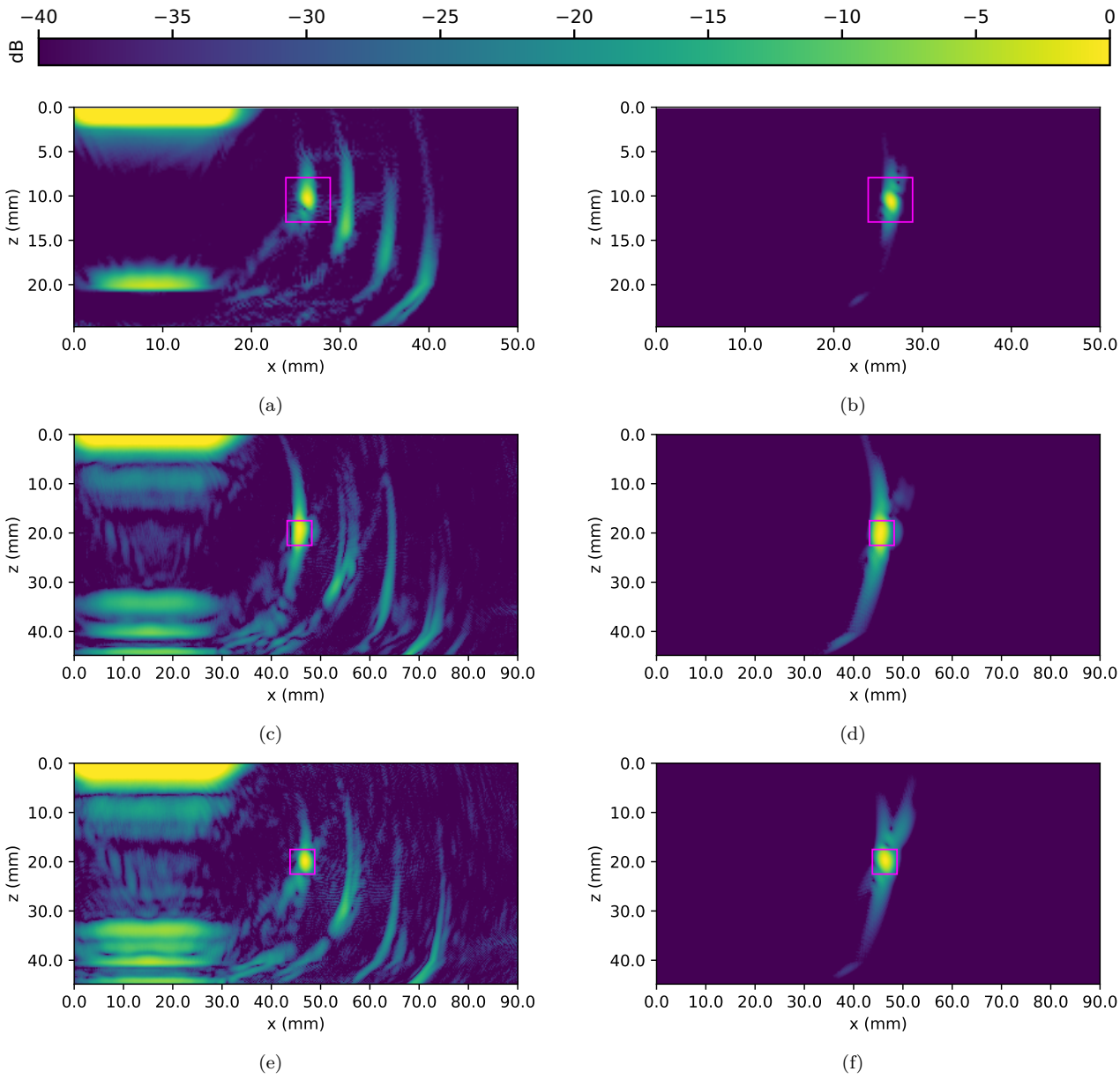

Figure 3. TFM images of view LL–T. Left column: experimental images $I_0(\boldsymbol{r})$. Right column: artefact-free simulated images $I_1(\boldsymbol{r}, \boldsymbol{y})$. Top row: crack. Middle row: notch. Bottom row: SDH. In each image, 0 dB corresponds to the maximum intensity in the magenta box.

sensitivity model is therefore 3 orders of magnitude faster than the multi-frequency analytical model. This significant speed-up is obtained because the sensitivity model provides only an *estimate* of the TFM intensity, under the single-frequency approximation and under the assumption that the intensity at the defect centre is representative of the actual peak intensity.

Finally, instead of computing the TFM intensities of a given defect type and orientation at different positions, this fast model could also conversely be used to quickly predict the TFM intensities of different defect types and orientations at one position, as an input for defect characterisation techniques. Its speed, flexibility and relative accuracy being crucial benefits.

V. Conclusion

A two-dimensional ray-based forward model for small defects was described and compared against FEM and experimental data for the inspection of a side-drilled hole, a crack and a notch. The model is used to predict

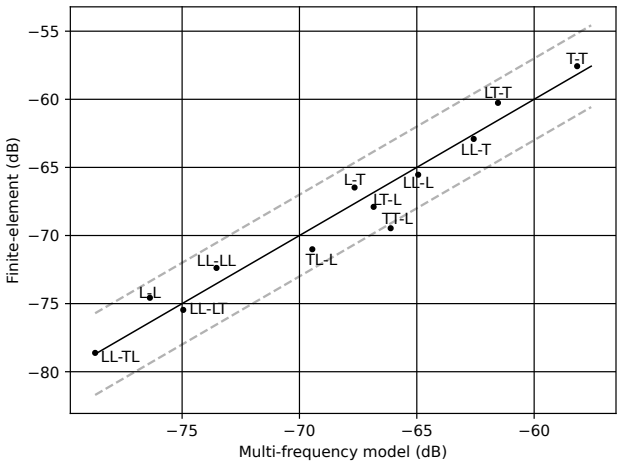

(a)

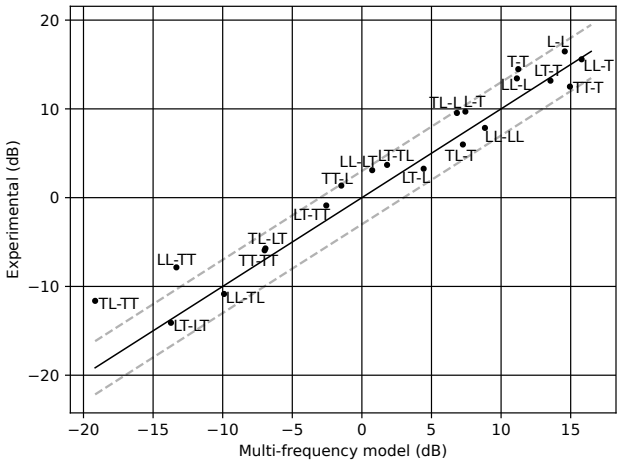

(b)

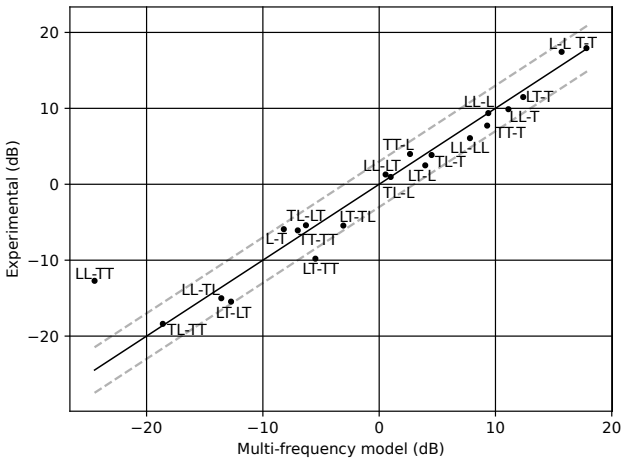

(c)

Figure 4. Comparison of the peak intensity scatterer responses in artefact-free multi-frequency images $I_1(\boldsymbol{r},\boldsymbol{y})$ and experimental/FEM images $I_0(\boldsymbol{r})$ for (a) a crack, (b) a notch, (c) a SDH. The solid black line corresponds to a perfect agreement. The dashed lines corresponds to an agreement of ± 3 dB. The 0 dB point is set arbitrarily.

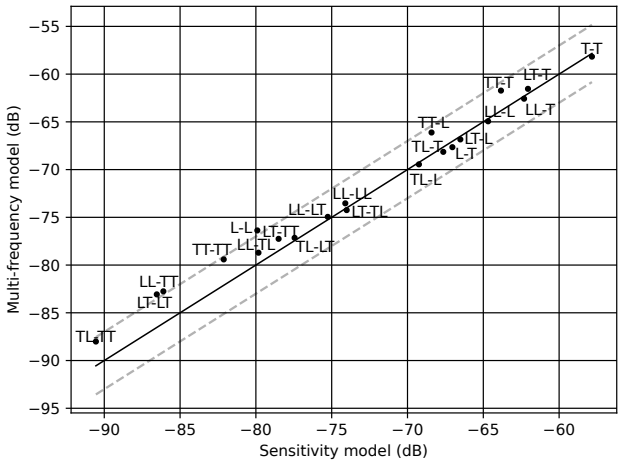

(a)

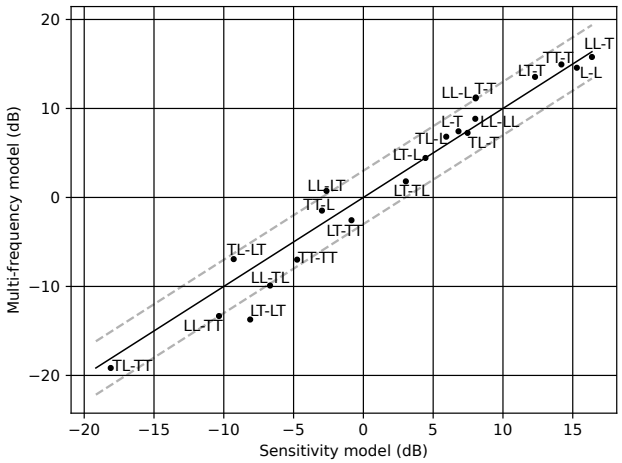

(b)

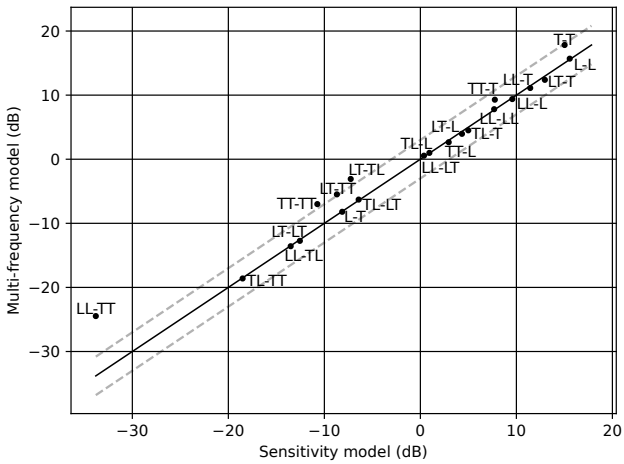

(c)

Figure 5. Comparison of sensitivity image $E(\boldsymbol{r})$ and simulated multi-frequency TFM image $I_1(\boldsymbol{r},\boldsymbol{y})$ for (a) a crack, (b) a notch, (c) a SDH. The 0 dB point is set arbitrarily.

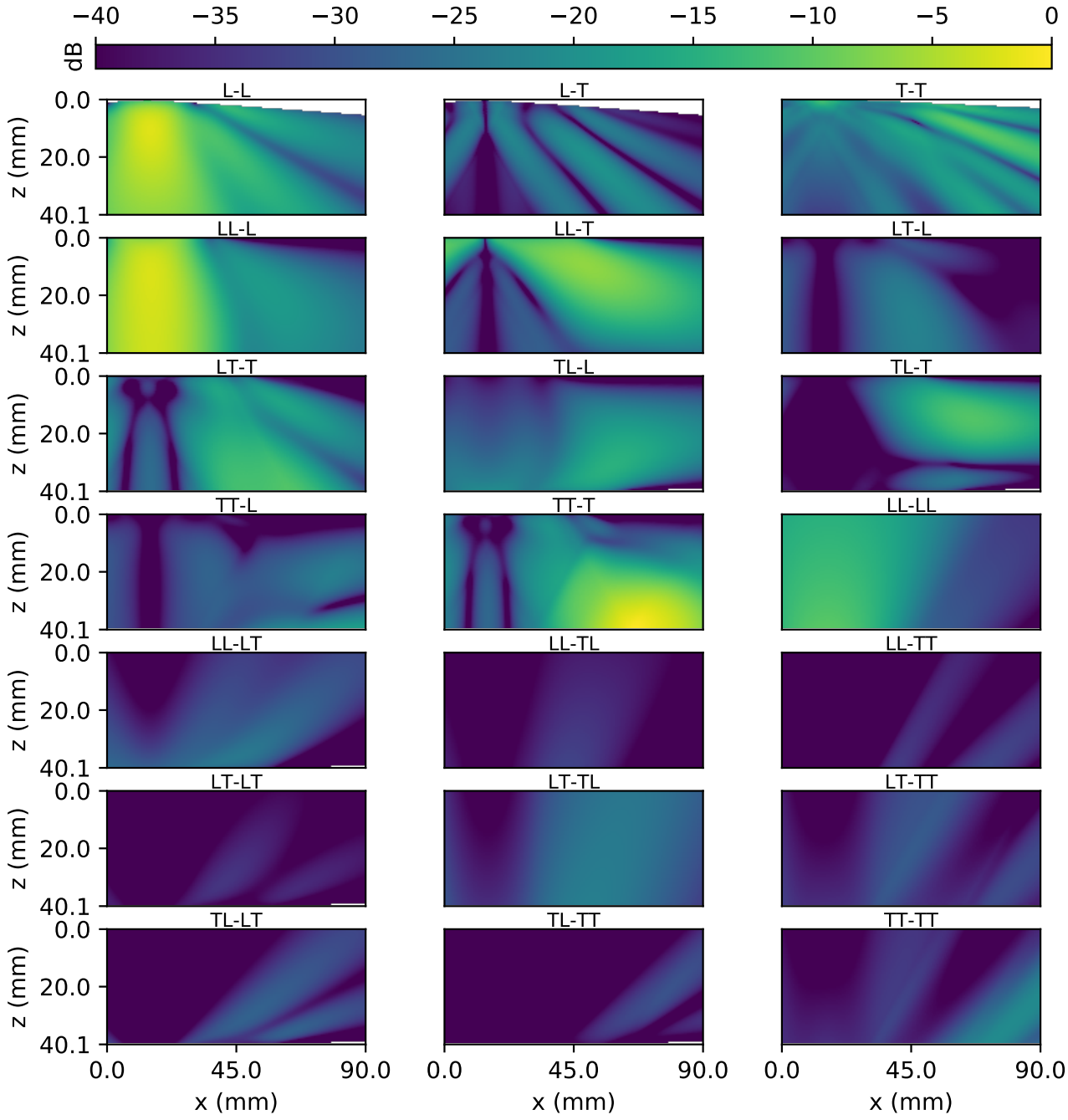

Figure 6. Sensitivity images (dB) for a 3×1 mm vertical notch.

artefact-free images of the defect. The model results are normalised against the measurements of the back wall echo. The model agrees with the experimental/FEM data within typically ±3 dB. Under a single-frequency assumption and assuming the maximum TFM intensify of the defect is at located at its centre, which is most often the case for small defects, a simpler model named the sensitivity model is derived. A typical ±3 dB agreement between this simple model and the fuller one is achieved. The sensitivity model is typically 3 orders of magnitude more computationally efficient and therefore is used to compute sensitivity images in less than two minutes, which are the predicted TFM intensities of a given defect in any view and anywhere. These images provide quantitative results to determine the views and the areas where a given defect type provide a large response. The sensitivity model was derived in this paper from a two-dimensional model but could be similarly obtained from a three-dimensional model; whether the agreement would remain acceptable has not been studied. In parallel work, the authors characterised the structural noise present in multi-view TFM images [32]; this will be combined with the sensitivity model developed in the current paper to provide quantitative estimates of the signal to noise ratio for any defect at any location in any view. This is a key input into any future data-fusion algorithm for improved defect detection and characterisation from multi-view TFM images.

Data access statement

Supporting data are openly available from data.bris under the DOI: 10.5523/XXX [will be added on paper acceptance]

Acknowledgements

The authors thank Dr Artem Kashubin (Imperial College London) for having provided the FEM results for the crack.

References

[1] B. W. Drinkwater and P. D. Wilcox, "Ultrasonic arrays for non-destructive evaluation: A review," *NDT & E International*, vol. 39, no. 7, pp. 525–541, Oct. 2006.

[2] H. Ammari, J. Garnier, W. Jing, H. Kang, M. Lim, K. Sølna, and H. Wang, *Mathematical and Statistical Methods for Multistatic Imaging*, ser. Lecture Notes in Mathematics. Cham: Springer International Publishing, 2013, vol. 2098.

[3] L. Borcea, G. Papanicolaou, C. Tsogka, and J. Berryman, "Imaging and time reversal in random media," *Inverse Problems*, vol. 18, no. 5, p. 1247, 2002.

[4] C. Holmes, B. W. Drinkwater, and P. D. Wilcox, "Post-processing of the full matrix of ultrasonic transmit–receive array data for non-destructive evaluation," *NDT & E International*, vol. 38, no. 8, pp. 701–711, 2005.

[5] J. Zhang, B. W. Drinkwater, P. D. Wilcox, and A. J. Hunter, "Defect detection using ultrasonic arrays: The multi-mode total focusing method," *NDT & E International*, vol. 43, no. 2, pp. 123–133, Mar. 2010.

[6] A. Fidahoussen, P. Calmon, M. Lambert, S. Paillard, and S. Chatillon, "Imaging of Defects in Several Complex Configurations by Simulation-helped Processing of Ultrasonic Array Data," in *AIP Conference Proceedings*, vol. 1211. AIP Publishing, Feb. 2010, pp. 847–854.

[7] R. Long, J. Russell, and P. Cawley, "Ultrasonic phased array inspection using full matrix capture," *Insight - Non-Destructive Testing and Condition Monitoring*, vol. 54, no. 7, pp. 380–385, Jul. 2012.

[8] Y. D. Zhang, X. Shen, R. Demirli, and M. G. Amin, "Ultrasonic Flaw Imaging via Multipath Exploitation," *Advances in Acoustics and Vibration*, vol. 2012, Jan. 2012.

[9] M. V. Felice, A. Velichko, and P. D. Wilcox, "Accurate depth measurement of small surface-breaking cracks using an ultrasonic array post-processing technique," *NDT & E International*, vol. 68, no. Supplement C, pp. 105–112, Dec. 2014.

[10] A. Fidahoussen, "Développement d'une méthode de reconstruction ultrasonore pour la localisation et la caractérisation de défauts," Ph.D. dissertation, Paris 11, Sep. 2012.

[11] S. Chatillon, S. Robert, P. Brédif, P. Calmon, G. Daniel, and F. Cartier, "Results of the 2014 UT modeling benchmark obtained with models implemented in CIVA: Solution of the FMC-TFM ultrasonic benchmark problem using CIVA," *AIP Conference Proceedings*, vol. 1650, no. 1, pp. 1847–1855, Mar. 2015.

[12] J. Zhang, T. Barber, A. Nixon, and P. Wilcox, "Investigation into distinguishing between small volumetric and crack-like defects using multi-view total focusing method images," *AIP Conference Proceedings*, vol. 1806, no. 1, p. 040003, Feb. 2017.

[13] F. Foroozan and S. ShahbazPanahi, "MUSIC-based array imaging in multi-modal ultrasonic non-destructive testing," in *2012 IEEE 7th Sensor Array and Multichannel Signal Processing Workshop (SAM)*, Jun. 2012, pp. 529–532.

[14] L. Le Jeune, S. Robert, E. L. Villaverde, and C. Prada, "Plane Wave Imaging for ultrasonic non-destructive testing: Generalization to multimodal imaging," *Ultrasonics*, vol. 64, pp. 128–138, Jan. 2016.

[15] J. F. Cruza, J. Camacho, and C. Fritsch, "Plane-wave phase-coherence imaging for NDE," *NDT & E International*, vol. 87, pp. 31–37, Apr. 2017.

[16] E. Iakovleva, S. Chatillon, P. Bredif, and S. Mahaut, "Multi-mode TFM imaging with artifacts filtering using CIVA UT forwards models," vol. 1581, Feb. 2014, pp. 72–79.

[17] N. Budyn, R. Bevan, A. J. Croxford, J. Zhang, P. D. Wilcox, A. Kashubin, and P. Cawley, "Sensitivity images for multi-view ultrasonic array inspection," *AIP Conference Proceedings*, vol. 1949, no. 1, p. 080001, Apr. 2018.

[18] R. B. Thompson and T. A. Gray, "A model relating ultrasonic scattering measurements through liquid–solid interfaces to unbounded medium scattering amplitudes," *The Journal of the Acoustical Society of America*, vol. 74, no. 4, pp. 1279–1290, Oct. 1983.

[19] L. W. Schmerr, *Fundamentals of Ultrasonic Nondestructive Evaluation: A Modeling Approach*, 2nd ed. New York, NY: Springer, May 2016.

[20] A. L. Lopez-Sanchez, H.-J. Kim, L. W. Schmerr, and A. Sedov, "Measurement Models and Scattering Models for Predicting the Ultrasonic Pulse-Echo Response From Side-Drilled Holes," *Journal of Nondestructive Evaluation*, vol. 24, no. 3, pp. 83–96, Sep. 2005.

[21] E. Glushkov, N. Glushkova, A. Ekhlakov, and E. Shapar, "An analytically based computer model for surface measurements in ultrasonic crack detection," *Wave Motion*, vol. 43, no. 6, pp. 458–473, Jun. 2006.

[22] A. Velichko and P. D. Wilcox, "A generalized approach for efficient finite element modeling of elastodynamic scattering in two and three dimensions," *The Journal of the Acoustical Society of America*, vol. 128, no. 3, pp. 1004–1014, Sep. 2010.

[23] A. Ben-Menahem and S. J. Singh, *Seismic Waves and Sources*. New York, NY: Springer New York, 1981.

[24] L. W. Schmerr, *Fundamentals of Ultrasonic Phased Arrays*, ser. Solid Mechanics and Its Applications. Cham: Springer International Publishing, 2015, vol. 215.

[25] L. W. Schmerr and S.-J. Song, *Ultrasonic Nondestructive Evaluation Systems*. Boston, MA: Springer US, 2007.

[26] C. Li, D. Pain, P. D. Wilcox, and B. W. Drinkwater, "Imaging composite material using ultrasonic arrays," *NDT & E International*, vol. 53, pp. 8–17, Jan. 2013.

[27] T. Stratoudaki, M. Clark, and P. D. Wilcox, "Laser induced ultrasonic phased array using full matrix capture data acquisition and total focusing method," *Optics Express*, vol. 24, no. 19, pp. 21 921–21 938, Sep. 2016.

[28] C. E. Duchon, "Lanczos Filtering in One and Two Dimensions," *Journal of Applied Meteorology*, vol. 18, no. 8, pp. 1016–1022, Aug. 1979.

[29] K. Turkowski, "Filters for common resampling tasks," in *Graphics gems*. Academic Press Professional, Inc., 1990, pp. 147–165.

[30] P. Huthwaite, "Accelerated finite element elastodynamic simulations using the GPU," *Journal of Computational Physics*, vol. 257, pp. 687–707, Jan. 2014.

[31] A. Kashubin and P. Cawley, "Simulation of Full Matrix Capture ultrasonic array data for immersion coupled inspection," in review.

[32] R. L. T. Bevan, J. Zhang, N. Budyn, A. J. Croxford, and P. D. Wilcox, "Experimental quantification of noise in linear ultrasonic imaging," *IEEE Transactions on Ultrasonics, Ferroelectrics, and Frequency Control*, pp. 1–1, 2018.

Appendix

a) Transmitter and scatterer in the same medium.: The beam-spread coefficient for the transmit path between the i-th element located at $\boldsymbol{x}_i$ and a scatterer located at $\boldsymbol{y}$ is defined here as:

$$B_i(\boldsymbol{y}) = \sqrt{\frac{1}{\|\boldsymbol{x}_i - \boldsymbol{y}\|}} \tag{10}$$

where $\|\cdot\|$ denotes the Euclidean distance. By symmetry the beam-spread coefficient for the receive path, $B_i'(\boldsymbol{y})$, is the same.

b) Beam-spread after one transmission.: We consider a first ray that starts from M_0 in medium 1, intersects the interface at the point M_1 and ends in M_2 in medium 2 after refraction (figure 7a). The Snell-Descartes law states that:

$$\frac{\sin\alpha_1}{\sin\beta_1} = \frac{c_1}{c_2}.$$

The quantity c_2 is either the longitudinal or the transverse wave speed in medium 2.

A second ray that leaves M_0 with a angle difference of $d\theta$ from the first ray intersects the interface at the point M_1'' and is also transmitted in medium 2 following the Snell-Descartes law. The beam that emerges in

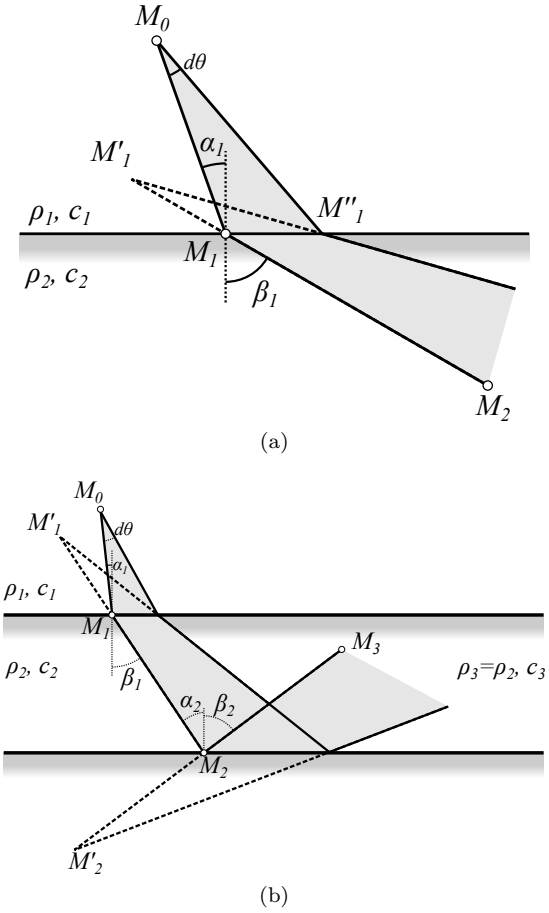

Figure 7. (a) Beam-spread after one interface. (b) Beam-spread after two interfaces.

medium 2 from the segment M_1M_1'' appears to come from a virtual point source M_1'. Using a first-order approximation for small $d\theta$ and the Snell-Descartes law, it can be shown that [24, B.2]:

$$|M_1'M_1| = \gamma_1|M_0M_1|$$

where $|\cdot|$ denotes here the Euclidean distance between two points and where

$$\gamma_1 \coloneqq \frac{c_1\cos^2\beta_1}{c_2\cos^2\alpha_1}.$$

The distance between the end point M_2 and the virtual source M_1' is therefore

$$|M_1'M_2| = \gamma_1|M_0M_1| + |M_1M_2| = \gamma_1|M_0M_1| + |M_1M_2|.$$

Conservation of energy dictates that the wave amplitude decreases in proportion to the square root of the separation between the rays and hence in inverse proportion to the square root of the distance from the virtual source:

$$B(M_2) = \sqrt{\frac{a}{\gamma_1|M_0M_1| + |M_1M_2|}}.$$

By continuity of the beam-spread at the interface:

$$\lim_{M_2 \to M_1} B(M_2) = \lim_{|M_1 M_2| \to 0} \sqrt{\frac{a}{\gamma_1 |M_0 M_1| + |M_1 M_2|}} = \sqrt{\frac{a}{\gamma_1 |M_0 M_1|}}.$$

Also:

$$\lim_{M_2 \to M_1} B(M_2) = B(M_1) = \sqrt{\frac{1}{|M_0 M_1|}}$$

so $a = \gamma_1$. This finally gives the the beam-spread coefficient after one transmission for the ray between the element $\boldsymbol{x}_i = M_0$ and the scatterer $\boldsymbol{y} = M_2$ is:

$$B_i(\boldsymbol{y}) = \sqrt{\frac{1}{|M_0 M_1| + |M_1 M_2|/\gamma_1}}. \tag{11}$$

By symmetry, the beam-spread coefficient for the reverse path is:

$$\begin{aligned} B_i'(\boldsymbol{y}) &= \sqrt{\frac{1}{|M_1 M_2| + |M_0 M_1|/\gamma_1'}} \\ &= \sqrt{\frac{1}{|M_1 M_2| + \gamma_1 |M_0 M_1|}} \end{aligned} \tag{12}$$

where

$$\gamma_1' \coloneqq \frac{c_2 \cos^2 \alpha_1}{c_1 \cos^2 \beta_1} = \frac{1}{\gamma_1}.$$

c) Beam-spread after multiple transmissions or reflections.: The general expression for multiple interfaces can be found recursively from equation (11); the demonstration is left to the reader.

Extending the notations introduced above, α_k is the incident angle at the k-th interface, β_k is the corresponding refracted/reflected angle, $\nu_k \coloneqq c_k / c_{k+1}$ is the k-th refractive index and γ_k is defined as:

$$\gamma_k \coloneqq \nu_k \frac{\cos^2 \beta_k}{\cos^2 \alpha_k} = \frac{\nu_k \cos^2 \beta_k}{1 - \nu_k^2 \sin^2 \beta_k} = \frac{\nu_k^2 - \sin^2 \alpha_k}{\nu_k \cos^2 \alpha_k}.$$

For a n-legged ray ($n-1$ interfaces), the beam-spread is:

$$B_i(\boldsymbol{y}) = \left(\sum_{k=0}^{n-1} \frac{|M_k M_{k+1}|}{\prod_{l=1}^{k} \gamma_l} \right)^{-1/2} \tag{13}$$

where $\boldsymbol{x}_i = M_0$ is the centre of the i-th array element and the scatterer is $\boldsymbol{y} = M_n$,